Hindawi
International Journal of Mathematics and Mathematical Sciences
Volume 2024, Article ID 2880748, 24 pages
https://doi.org/10.1155/2024/2880748

Research Article

Investigation of Magnetized Casson Nanofluid Flow along Wedge: Gaussian Process Regression

M. Shanmugapriya,[1] R. Sundareswaran,[1] S. Gopi Krishna,[2] and Abdu Alameri[3]

[1]*Department of Mathematics, Sri Sivasubramaniya Nadar College of Engineering, Chennai 603110, India*
[2]*Department of Mathematics, Rajalakshmi Engineering College, Thandalam, Chennai 602105, India*
[3]*Department of Biomedical Engineering, Faculty of Engineering, University of Science and Technology, Sana'a, Yemen*

Correspondence should be addressed to Abdu Alameri; a.alameri2222@gmail.com

Received 27 August 2023; Revised 23 November 2023; Accepted 21 December 2023; Published 8 January 2024

Academic Editor: Saranya Shekar

An unsteady two-dimensional magnetized Casson nanofluid flow model is constructed over a wedge under the effect of thermal radiation and chemical reaction. The multiple slip effects are also assumed near the surface of the wedge along with the convective boundary restrictions. This study investigates the application of soft computing techniques to address the challenges posed by the complexity of problem modeling and numerical methods. Traditional approaches incorporating various model factors may struggle to provide accurate solutions. To resolve this issue, Gaussian process regression (GPR) is employed to predict the solution of the proposed flow model. With the help of the numerical shooting method together with Runge–Kutta–Fehlberg fourth-fifth-order (RKF-45) reference data, the GPR model is trained. The numerical simulation illustrated that the Casson fluid parameter (β) and the unsteadiness parameter (S) strengthen the friction factor, and the heat transfer rate is enhanced as the radiation parameter (R_d) becomes larger. In addition, the Biot numbers (Bi_1 & Bi_2) lead to strengthen nanoparticle temperature; an opposite behavior is noticed with the skin friction coefficient ($\widetilde{S}_{fx}Re_x^{0.5}$), heat transfer rate ($\widetilde{H}_{tx}\,Re_x^{0.5}$), and nanoparticle transfer rate ($\widetilde{C}_{tx}Re_x^{0.5}$). The GPR model with the exponential Kernel function provided better performance than other functions on both training and checking datasets to predict $\widetilde{S}_{fx}Re_x^{0.5}$, $\widetilde{H}_{tx}\,Re_x^{0.5}$, and $\widetilde{C}_{tx}Re_x^{0.5}$. Statistical metrics including RMSE, MAE, MAPE, MSE, R^2, and R are employed to check the accuracy and convergences of the predicted and numerical solutions obtained through GPR and RKF-45. It is observed that all three GPR models had an R^2 value of higher than 0.9. The proposed study demonstrates the advantages of employing soft computing methods (GPR) to effectively analyse the behavior of complex flow models.

1. Introduction

Aerospace engineering and fluid mechanics both benefit significantly from the study of fluid flow over a wedge because they offer important insights into how fluids behave when they interact with solid surfaces. This knowledge aids in the comprehension of boundary layer dynamics, aerodynamic phenomena, and the design of airfoil shapes for effective lift and drag characteristics in a variety of engineering applications. Recently, the study of MHD boundary layer slip flow of heat and mass transfer performance over a wedge-shaped geometry has been extensively explored due to its wide applications in science and engineering. It is used in industrial processes, including geothermal systems, nuclear reactors, nuclear waste storage, thermal insulation in aircraft cabins, and heat exchangers. Earlier in 1931, Falkner and Skan [1] investigated the flow over a static wedge immersed in a viscous fluid and developed the Falkner–Skan equation. Awaludin et al. [2] discovered the repercussions of a magnetic field on the flow of an incompressible and electrically conducting fluid past a stretching/shrinking wedge. The viscous dissipation effects on the MHD boundary layer stream of nanofluid across a wedge embedded in porous medium were examined numerically via

the spectral quasilinearization method (SQLM) by Ibrahim and Tulu [3]. A few inquiries involving the Falkner–Skan flow with various types of physical characteristics past a wedge can be found in the studies of Kudenatti and Amrutha [4], Haq et al. [5], and Butt et al. [6].

The study of non-Newtonian fluid model has gained an incredible position among researchers because of their applications in industries and chemical engineering process, such as petroleum and polymer industries, food technology, heat exchangers, paper production, and electronic cooling system. Biological fluids (blood, salvia, etc.) and foodstuffs (honey, jellies, jams, soups, etc.) are examples of non-Newtonian fluids because of their physical nature. Casson fluid is a type of non-Newtonian fluid that behaves like an elastic solid. Casson model constitutes a fluid model that exhibits shear thinning characteristics, yield stress, and high shear viscosity [7]. These fluids are applied in technical processes, such as biomedical and industrial engineering, energy generation, dynamics, and geophysical fluid mechanics. Hussanan et al. [8], Khan et al. [9], Ullah et al. [10], Ullah et al. [11], and Guadagni et al. [12] have scrutinized the consequence of magnetic field, Soret–Dufour, viscous dissipation, and chemical reactions on the Casson fluid in different flow settings. Mukhopadhyay and Mandal [13] developed a numerical study of the boundary layer forced convection flow of a Casson fluid over a symmetric porous wedge. They found that the Casson fluid parameter tends to control the flow separation. El-dabe et al. [14] used the numerical method (finite difference method) to obtain the solution of the MHD boundary layer flow of Casson fluid on a moving wedge with heat and mass transfer. Mahdy [15] illustrated the impact of slip at the boundary of unsteady two-dimensional MHD flow of a Casson fluid over a stretching surface using the very robust computer algebra software MATLAB. From their results, it was observed that the velocity increases and the thermal boundary layer becomes thinner with the increasing slip parameter. Raju and Sandeep [16] used the Runge–Kutta and Newton's methods to obtain the solution of MHD slip flow of a dissipative Casson fluid over a moving wedge with heat source/sink. Recently, researchers focused on investigating the sundry flow features of Casson nanofluid in different frames [17–20].

One of the massive challenges within the modern science and technology panorama is attaining concrete enhancements regarding the rate of heat transfer of ordinary fluids such as water, lubricants, oils, ethylene glycol, biological fluids, and toluene. These fluids have low thermal conductivity. To enhance the thermal conductivity of regular fluids, Choi[21] were the first who award a novel cohort of heat transfer fluid that is developed by dissolving non-metallic or metallic tiny particles with a size of under 100 nm in an ordinary fluid. The components of the nanoparticles include chemically stable metals (gold and copper), metal oxides (alumina, zirconia, titania, and silica), metal carbides (SiC), oxide ceramics (Al_2O_3, CuO, TiO_2, and SiO_2), metal nitrides (SiN and AIN), carbon in various forms (fullerene, diamond, graphite, carbon nanotubes, and graphene), and other functionalized nanoparticles. The nanofluids can augment the thermal conductivity and upgrade the heat transfer efficiency of ordinary fluids. Nanofluids are used in different fields, including generator cooling, engine and transformer cooling, solar heating, nuclear system cooling, electronic cooling, vehicle thermal management, lubrication, refrigeration, thermal storage, defense, space, biomedical, heat pipe, ships, and drug reduction. A two-phase model with the roles of Brownian diffusion and thermophoresis as slip mechanisms was proposed by Buongiorno [22]. Mustafa [22] demonstrated the insignificant impact of Brownian movement on heat transfer while illuminating the slip influence for rotating flow using the Buongiorno model. A few studies involving the consequence of Brownian and thermophoresis on different types of nanofluid have been specified in Makkar [23], Song et al. [24], and Ragupathi et al. [25].

In today's world, artificial intelligence (AI) techniques, such as artificial neural network (ANN), adaptive neuro-fuzzy inference system (ANFIS), multiple adaptive neuro-fuzzy inference system (MANFIS), group method of data handling (GMDH), category and regression tree (CART), support vector machine (SVM), genetic algorithm (GA), and particle swarm optimization (PSO), play a vital role for solving system of nonlinear complex models in every domain of science and engineering. Recently, numerous researchers have explored these new computational methods (AI technology) to predict the output responses of nonlinear complex systems. Among those, Gaussian process regression (GPR) is one of the AI techniques to forecast the result responses of nonlinear complex systems. These models have widespread application due to their outstanding performance in practice and attractive analytical features, such as machining optimization, machining optimization, analytical sensor calibration, and rehabilitation engineering. Sharma et al. [26] developed an artificial neural network (ANN) model to investigate Darcy–Forchheimer hybrid nanofluid flow heat transfer through a rotating Riga disk. The effect of chemical reaction is also included, and a high-performance accurate ANN model was trained to predict thermal energy transfer performance. Raja et al. [28] investigated the 3D hybrid nanofluid flow over biaxial porous stretching/shrinking sheet with heat transfer, radiative heat, and mass flux solved through Bayesian regularization technique based on backpropagation neural networks. Computational fluid dynamic (CFD) AI techniques were employed for Casson nanofluid [29], MHD Carreau nanofluid flow containing gyrotactic microorganisms [30], biomagnetic ternary hybrid nanofluid [31], MHD Sutterby hybrid nanofluid flow with activation energy [32], and nonlinear radiative magnetized Carreau nanofluid [33].

From the above literature survey, no attempt has been discussed before on the presented physical model for multiple slip flow of magnetized Casson nanofluid over a wedge. The following significant characteristics can be used to highlight the goals, novelty, contributions, and insights of the research analysis that have been introduced:

(i) The present study introduces an innovative approach to investigate heat transport in fluid models by combining soft computing techniques with numerical computing through the GPR model

(ii) An unsteady, incompressible, laminar, viscous, and magnetized Casson nanofluid flow model over a wedge under the effect of thermal radiation, chemical reaction, and multiple slip features with first-order relations is considered

(iii) A dataset is constructed through mathematical simulation (Runge–Kutta–Fehlberg fourth-fifth-order method along with shooting technique) for analyzing dimensionless quantities of engineering interest

(iv) Convergence of the developed GPR results is examined through statistical metrics, including root mean square error (RMSE), mean absolute error (MAE), mean absolute percentage error (MAPE), mean square error (MSE), coefficient of determination (R^2), and correlation coefficient (R)

(v) Considering statistical metrics such as RMSE, MAE, MAPE, and MSE , the developed GPR models are more accurate in predicting $\widetilde{S}_{fx}Re_x^{0.5}$, $\widetilde{H}_{tx}\,Re_x^{0.5}$, and $\widetilde{C}_{tx}Re_x^{0.5}$ values

1.1. Applications. The study of magnetized Casson nanofluid flow along a wedge using Gaussian process regression (GPR) combines the concept of fluid dynamics, nanotechnology, and machine learning. This study is potential contributions to optimizing processes and systems in various industries, ranging from material processing and energy systems to biomedical applications and environmental engineering. Also, this study provides valuable insights that can be leveraged to improve the efficiency and effectiveness of diverse applications where complex fluid dynamics play a crucial role.

2. Modeling

MHD Casson nanofluid flow model over a wedge-shaped geometry with thermal radiation, chemical reaction, and slip effects is considered. The flow over the wedge with velocity $\widetilde{u}_w^*(x,t) = \widetilde{U}_w^*\widetilde{x}^m/1-\widetilde{\varepsilon}t$ and the free stream velocity $\widetilde{u}_e^*(x,t) = \widetilde{U}_{fs}^*\widetilde{x}^m/1-\widetilde{\varepsilon}t$ is the free stream, where $\widetilde{U}_w^*, \widetilde{U}_{fs}^*, \widetilde{\varepsilon}, m$ are positive constants and t is the time. Here, $m = \beta_1/(2-\beta_1), \beta_1$ is the wedge angle parameter that corresponds to $\beta_1 = \widetilde{\Omega}^*/\pi$ for the total wedge angle $\widetilde{\Omega}^*$. Temperature and nanoparticle fraction at the wall are $\widetilde{T}_w$ and $\widetilde{C}_w$, respectively, and these are greater than that of free stream $\widetilde{T}_{fs}$ and $\widetilde{C}_{fs}$, respectively. The variable magnetic field $B(x,t) = \widetilde{B}_0^* x^{0.5(m-1)}/(1-\widetilde{\varepsilon}t)^{0.5}$ was applied to the flow direction. Figure 1 depicts the mechanism of flow structure.

Cauchy stress tensor $\widetilde{\tau}^{*1/q}$ for the Casson fluid model is defined by Raju and Sandeep [16]:

$$\widetilde{\tau}^{*1/q} = \widetilde{\tau}_0^{*1/q} + \mu\widetilde{\gamma}^{*1/q}, \tag{1}$$

$$\widetilde{\tau}_{ij}^* = \begin{cases} 2\left(\mu_b + \dfrac{P_y}{\sqrt{2\pi}}\right)\widetilde{e}_{ij}^*, & if\ \pi > \pi_c, \\ 2\left(\mu_b + \dfrac{P_y}{\sqrt{2\pi_c}}\right)\widetilde{e}_{ij}^*, & if\ \pi < \pi_c, \end{cases} \tag{2}$$

where

$$\widetilde{e}_{ij}^* = \frac{1}{2}\left(\frac{\partial\widetilde{u}_i}{\partial x_j} + \frac{\partial\widetilde{u}_j}{\partial x_i}\right), \tag{3}$$

in which μ_b = plastic dynamic viscosity, $P_y = \mu_b\sqrt{2\pi}/\beta$ =yield stress of the fluid, $\pi = \widetilde{e}_{ij}^*\widetilde{e}_{ij}^*$ = product of the rate of strain tensor with itself, $\widetilde{e}_{ij}^*$ =deformation rate, π_c = critical value based on Casson non-Newtonian model, and $\widetilde{u}_i$ = velocity components. Following Song et al. [25], Animasaun et al. [34],and Cao et al. [35], the modification of Buongiorno's nanofluid model was considered in the energy equation and concentration equation since thermomigration and haphazard motion of nanoparticles occur due to variation in the concentration. Based on the aforesaid deliberation, the fluid transport equations become (Hussanan et al. [8], Khan et al. [9], and Ullah et al. [11])

$$\frac{\partial\widetilde{u}}{\partial x} + \frac{\partial\widetilde{v}}{\partial y} = 0, \tag{4}$$

$$\frac{\partial\widetilde{u}}{\partial t} + \widetilde{u}\frac{\partial\widetilde{u}}{\partial x} + \widetilde{v}\frac{\partial\widetilde{u}}{\partial y} = \frac{\partial\widetilde{u}_e}{\partial t} + \widetilde{u}_e\frac{\partial\widetilde{u}_e}{\partial x} + \vartheta\left(1+\frac{1}{\beta}\right)\frac{\partial^2\widetilde{u}}{\partial y^2} - \left[\frac{\sigma B^2(x,t)}{\rho} + \left(1+\frac{1}{\beta}\right)\frac{\vartheta\varphi}{k_p}\right](\widetilde{u}-\widetilde{u}_e), \tag{5}$$

$$\frac{\partial\widetilde{T}}{\partial t} + \widetilde{u}\frac{\partial\widetilde{T}}{\partial x} + \widetilde{v}\frac{\partial\widetilde{T}}{\partial y} = \frac{\kappa}{\rho c_p}\frac{\partial^2\widetilde{T}}{\partial y^2} + \frac{\vartheta}{c_p}\left(1+\frac{1}{\beta}\right)\left(\frac{\partial\widetilde{u}}{\partial y}\right)^2 + \frac{(\rho c)_p}{(\rho c)_f}\left[\frac{D_B}{\Delta C}\frac{\partial\widetilde{C}}{\partial y}\frac{\partial\widetilde{T}}{\partial y} + \frac{D_T}{T_{fs}}\left(\frac{\partial\widetilde{T}}{\partial y}\right)^2\right] + \frac{16\sigma^*\widetilde{T}_{fs}^3}{3k^*\rho c_p}\left(\frac{\partial^2\widetilde{T}}{\partial y^2}\right), \tag{6}$$

$$\frac{\partial\widetilde{C}}{\partial t} + \widetilde{u}\frac{\partial\widetilde{C}}{\partial x} + \widetilde{v}\frac{\partial\widetilde{C}}{\partial y} = D_B\left(\frac{\partial^2\widetilde{C}}{\partial y^2}\right) + \frac{D_T\Delta C}{\widetilde{T}_{fs}}\left(\frac{\partial^2\widetilde{T}}{\partial y^2}\right) - k_c(x,t)\left(\widetilde{C}-\widetilde{C}_{fs}\right), \tag{7}$$

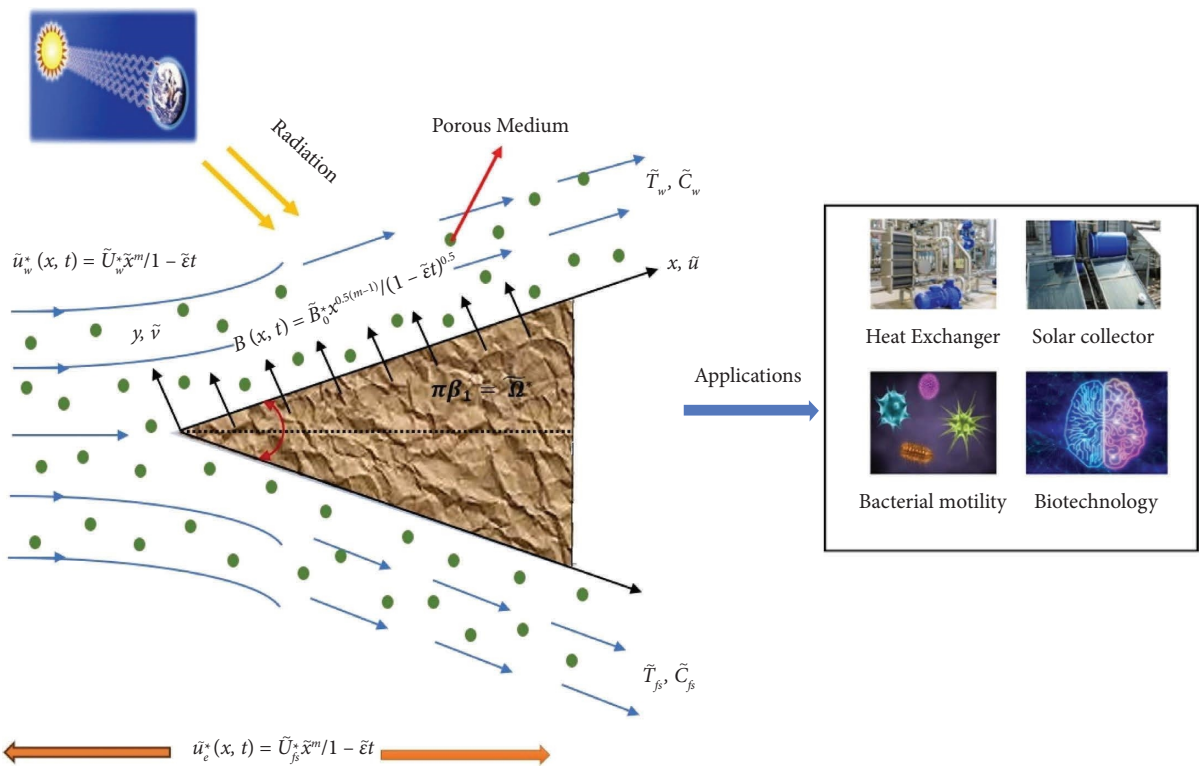

Figure 1: Physical diagram for the flow system.

where $\vartheta = \mu/\rho, k_p(x,t) = k_1(1-\tilde{\varepsilon}t)/x^{m-1}, k_c(x,t) = ak_1 x^{m-1}/(1-\tilde{\varepsilon}t), \beta \longrightarrow \infty$ and $\beta > 0, \beta < 0$ indicates the Newtonian and non-Newtonian fluid models, respectively.

The corresponding boundary restrictions with slip conditions are as follows:

$$t < 0; \quad \tilde{u} = \tilde{v} = 0, \tilde{T} = \tilde{T}_{fs}, \tilde{C} = \tilde{C}_{fs} \quad \text{for any} \quad x, y, \tag{8}$$

$$\left.\begin{aligned} &t \geq 0;\ \tilde{u} = \tilde{u}_w(x,t) + N_1(x,t)\gamma\left(1 + \frac{1}{\beta}\right)\frac{\partial \tilde{u}}{\partial y}, \\ &\tilde{v} = 0, -k_f \frac{\partial \tilde{T}}{\partial y} = h_f(x,t)\left(\tilde{T}_w - \tilde{T}\right), -k_f \frac{\partial \tilde{C}}{\partial y} = h_s(x,t)\left(\tilde{C}_w - \tilde{C}\right), \end{aligned}\right\} at\ y = 0, \tag{9}$$

$$\tilde{u} \longrightarrow \tilde{u}_e(x,t), \tilde{T} \longrightarrow \tilde{T}_{fs}, \tilde{C} \longrightarrow \tilde{C}_{fs} \text{ as } \quad y \longrightarrow \infty, \tag{10}$$

where $N_1(x,t) = N_0 x^{-0.5(m-1)}(1-\tilde{\varepsilon}t)^{0.5}$, $h_f(x,t) = h_0 x^{0.5(m-1)}(1-\tilde{\varepsilon}t)^{-0.5}$, and $h_s(x,t) = h_1 x^{0.5(m-1)}(1-\tilde{\varepsilon}t)^{-0.5}$ with N_0, h_0, and h_1 being constants. Suitable similarity variables are introduced as follows:

$$\left.\begin{aligned}
\psi &= \left[\frac{2\vartheta\widetilde{U}_{fs}}{(m+1)(1-\widetilde{\varepsilon}t)}\right]^{0.5} x^{0.5(m+1)} f(\zeta),\\
\zeta &= \left[\frac{(m+1)\widetilde{U}_{fs}}{2\vartheta(1-\widetilde{\varepsilon}t)}\right]^{0.5} x^{0.5(m-1)} y, \widetilde{u} = \frac{\widetilde{U}_{fs}}{(1-\widetilde{\varepsilon}t)} x^m f',\\
\widetilde{v} &= \left[\frac{(m+1)\vartheta\widetilde{U}_{fs}}{2(1-\widetilde{\varepsilon}t)}\right]^{0.5} x^{0.5(m-1)} \left[f(\zeta) + \zeta\left(\frac{m-1}{m+1}\right) f'(\zeta)\right],\\
\theta(\zeta) &= \frac{\widetilde{T}-\widetilde{T}_{fs}}{\widetilde{T}_w-\widetilde{T}_{fs}}, \varphi(\zeta) = \frac{\widetilde{C}-\widetilde{C}_{fs}}{\widetilde{C}_w-\widetilde{C}_{fs}}, \widetilde{u} = \frac{\partial\psi}{\partial y}, \widetilde{v} = \frac{-\partial\psi}{\partial x}.
\end{aligned}\right\}, \tag{11}$$

The stream function ψ satisfies equation (1). Under the transformations, equations (5)–(10) yield

$$\left(1+\frac{1}{\beta}\right) f''' + f f'' + \frac{2m}{m+1}\left(1-f'^2\right) + S\frac{2}{m+1}\left(1-f'-0.5\zeta f''\right) - \frac{2}{m+1}\left[M-\left(1+\frac{1}{\beta}\right)K\right]\left(f'-1\right) = 0, \tag{12}$$

$$\frac{1}{\Pr}\left[1+\frac{4}{3}R_d\right]\theta'' + f\theta' - \frac{4m}{m+1} f'\theta + \left(1+\frac{1}{\beta}\right)\mathrm{Ec}f''^2 - S\left[\frac{4m}{m+1}\theta + \frac{1}{m+1}\zeta\theta'\right] + Nb\varphi'\theta' + Nt\theta'^2 = 0, \tag{13}$$

$$\frac{\varphi''}{Le} + f\varphi' - \frac{4m}{m+1} f'\varphi - S\left[\frac{4m}{m+1}\varphi + \frac{1}{m+1}\zeta\varphi'\right] + \frac{Nt}{Nb}\theta'' - \frac{2}{m+1}R\varphi = 0, \tag{14}$$

and the associated boundary restrictions become

$$\left.\begin{aligned}
&f(\zeta) = 0, f'(\zeta) = \gamma + \delta\left(\frac{m+1}{2}\right)^{0.5}\left(1+\frac{1}{\beta}\right) f''(\zeta),\ \theta'(\zeta) = -Bi_1\left(\frac{2}{m+1}\right)^{0.5}(1-\theta(\zeta)),\\
&\varphi'(\zeta) = -Bi_2\left(\frac{2}{m+1}\right)^{0.5}(1-\varphi(\zeta)) \text{ at } \zeta = 0,
\end{aligned}\right\}, \tag{15}$$

$$f'(\zeta) = 1, \theta(\zeta) = 0, \varphi(\zeta) = 0 \text{ at } \zeta \longrightarrow \infty, \tag{16}$$

where the governing parameters are as follows:

$$\left.\begin{aligned}
&S=\frac{\tilde{\varepsilon}x^{1-m}}{\tilde{U}_{fs}}, M=\frac{\sigma B_0^2}{\rho\tilde{U}_{fs}}, K=\frac{\vartheta\varphi}{k_1\tilde{U}_{fs}}, \Pr=\frac{\mu c_p}{\kappa}, R_d=\frac{4\sigma^*\tilde{T}_{fs}^3}{kk_1^*}R=\frac{\vartheta a k_2}{\tilde{U}_{fs}},\\
&Ec=\frac{\tilde{u}_e^2}{c_p\left(\tilde{T}_w-\tilde{T}_{fs}\right)}, Nb=\frac{\tau D_B\left(\tilde{C}_w-\tilde{C}_{fs}\right)}{\vartheta\Delta C}, Nt=\frac{\tau D_T\left(\tilde{T}_w-\tilde{T}_{fs}\right)}{\tilde{T}_{fs}\vartheta}, Le=\frac{\vartheta}{D_B},\\
&\gamma=\frac{U_w}{U_{fs}}, \delta=N_0\sqrt{U_{fs}\gamma}, Bi_1=\frac{h_0}{k_f}\sqrt{\frac{\gamma}{U_{fs}}}, Bi_2=\frac{h_1}{k_f}\sqrt{\frac{\gamma}{U_{fs}}},
\end{aligned}\right\}, \tag{17}$$

where Le, γ, δ, Bi_1, and Bi_2 are, respectively, Lewis number, moving wedge parameter, slip parameter, and Biot numbers. Skin friction coefficient $\tilde{S}_{fx}=\tilde{\tau}_w/\rho\tilde{u}_e^2$, heat transfer rate $\tilde{H}_{tx}=\tilde{x}q_w/k(\tilde{T}_w-\tilde{T}_{fs})$, and nanoparticle transfer rate $\tilde{C}_{tx}=\tilde{x}d_w/D_B(\tilde{C}_w-\tilde{C}_{fs})$ at the wall $((ie)\zeta=0)$ are defined as follows:

$$\left.\begin{aligned}
&\tilde{S}_{fx}Re_x^{0.5}=\sqrt{\frac{m+1}{2}}\left(1+\frac{1}{\beta}\right)\frac{\partial^2 f}{\partial\zeta^2},\\
&\tilde{H}_{tx}\,Re_x^{-0.5}=-\sqrt{\frac{m+1}{2}}\left[1+\frac{4}{3}R_d\right]\frac{\partial\theta}{\partial\zeta},\\
&\tilde{C}_{tx}Re_x^{-0.5}=-\sqrt{\frac{m+1}{2}}\ \frac{\partial\varphi}{\partial\zeta},
\end{aligned}\right\}, \tag{18}$$

where $Re_x=\tilde{u}_{e\tilde{x}}/\vartheta$ is the Reynolds number.

3. Methodology

In this study, two methodologies, namely, shooting technique together with Runge–Kutta–Fehlberg 4-5th order (RKF-45) and Gaussian process regression (GPR), have been used to perform the mathematical and soft technique simulation for the flow of magnetized Casson nanofluid over a wedge. The numerical approach of RFK-45 and the background of the GPR model were explained briefly in this section.

3.1. Mathematical Simulation

3.1.1. Explanation of the RKF-45 Scheme. The system of nonlinear differential equations (12)–(14) with the boundary restrictions equations (15) and (16) are solved mathematically with the assistance of shooting technique together with Runge–Kutta–Fehlberg fourth-fifth-order integration scheme. The mathematical simulation of the RKF-45 scheme is presented in Figure 2. Initially, we reduce the order of the equation by using the following procedure:

$$\left.\begin{aligned}
&f=u_1, f'=u_2, f''=u_3, f'''=u_3',\\
&\theta=u_4, \theta'=u_5, \varphi=u_6, \varphi'=u_7,\\
&u_3'=\frac{-1}{(1+1/\beta)}\left\{u_1u_3+\frac{2m}{m+1}\left(1-u_3^2\right)+S\frac{2}{m+1}\left(1-u_2-0.5\zeta u_3\right)-\frac{2}{m+1}\left[M-\left(1+\frac{1}{\beta}\right)K\right](1-u_2)\right\},\\
&u_5'=\frac{-\Pr}{[1+4/3R_d]}\left\{u_1u_5-\frac{4m}{m+1}u_2u_4+\left(1+\frac{1}{\beta}\right)\mathrm{Ec}u_3^2-S\left[\frac{4m}{m+1}u_4+\frac{1}{m+1}\zeta u_5\right]+\mathrm{Nb}u_7u_5+\mathrm{Nt}u_5^2\right\},\\
&u_7'=-Le\left\{u_1u_7-\frac{4m}{m+1}u_2u_6-S\left[\frac{4m}{m+1}u_6+\frac{1}{m+1}\zeta u_7\right]+\frac{Nt}{Nb}u_5'-\frac{2}{m+1}Ru_6\right\},
\end{aligned}\right\}, \tag{19}$$

with the boundary restrictions

$$\left.\begin{aligned} & u_1(\zeta)=0,\ u_2(\zeta)=\gamma+\delta\left(\frac{m+1}{2}\right)^{0.5}\left(1+\frac{1}{\beta}\right)u_3(\zeta), u_3(\zeta)=a_1,\ u_4(\zeta)=1+\frac{1}{Bi_1}\left(\frac{m+1}{2}\right)^{0.5}u_5(\zeta), \\ & u_5(\zeta)=a_2, u_6(\zeta)=1+\frac{1}{Bi_2}\left(\frac{m+1}{2}\right)^{0.5}u_7(\zeta),\ u_7(\zeta)=a_3 \text{ at } \zeta=0, \\ & u_2(\zeta)=1,\ u_4(\zeta)=0,\ u_6(\zeta)=0 \text{ at } \zeta\longrightarrow\infty. \end{aligned}\right\}, \tag{20}$$

The numerical simulation is performed until the result is corrected up to the desired accuracy of 10^{-6} level.

3.1.2. Value of $\widetilde{S}_{fx}Re_x^{0.5}$ and $\widetilde{H}_{tx}Re_x^{0.5}$ with Variation of m and Pr. Owing to this validity of solution, a comparative investigation of $\widetilde{S}_{fx}Re_x^{0.5}$ for various values of m and $\widetilde{H}_{tx}Re_x^{0.5}$ for various values of Pr with earlier published results (Ishak et al. [36] and Ullah et al. [37]; Kuo [38] and Raju and Sandeep [16]) is reported in Tables 1 and 2 which validate the current code.

3.2. Soft Technique Simulation

3.2.1. Explanation of the GPR Model. Gaussian process regression (GPR) is one of the nonparametric learning algorithms which can model highly complex systems. Every finite subset of data produced by the Gaussian process in a certain domain can adhere to a multidimensional Gaussian distribution. For a given set of n observations training samples, $S=\{(x_i,y_i)|i=1,2,\ldots n\}$, where $x_i\in\mathscr{R}^n$ is the input vector and $y_i\in\mathscr{R}$ is the corresponding output. Thus, a Gaussian process (GP) is a collection of random variables $\mathscr{G}(x)$ and is defined as follows:

$$\mathscr{G}(x)\sim GP\left(m(x),\mathscr{k}\left(x,x'\right)\right), \tag{21}$$

where $m(x)=\mathrm{E}[\mathscr{G}(x)]$ represents the mean function of the prior knowledge about the latent function for variable x and $\mathscr{K}(x,x')=\mathrm{E}[(\mathscr{G}(x)-m(x))(\mathscr{G}(x')-m(x'))]$ denotes the covariance or kernel function of the confidence level for $m(x)$. Usually, the value of the mean function of the equation is considered to be 0 in most applications. The relation between the input vector (x_i) of each data point and its output (y_i) value in the GP is defined as follows:

$$y_i=\mathscr{G}(x_i)+\epsilon, \tag{22}$$

where ϵ denotes the Gaussian distribution noise value that has 0 mean and σ^2 variance $(ie)\epsilon\sim N(0,\sigma^2)$.

Moreover, $\mathscr{G}=[\mathscr{G}(x_1),\mathscr{G}(x_2)\ldots\ldots\mathscr{G}(x_n)]^T$ also displays Gaussian behavior, defined as $p(\mathscr{G}|x_i)=N(0,\mathscr{K})$. Here, the covariance matrix $\mathscr{K}$ has $\mathscr{K}_{ij}=\mathscr{k}(x_i,x_j)$ components.

$$\mathscr{K}(x,S)=\begin{bmatrix} \mathscr{k}(x_1,x_1) & \mathscr{k}(x_1,x_2) & \mathscr{k}(x_1,x_3) & \cdots & \mathscr{k}(x_1,x_n) \\ \mathscr{k}(x_2,x_1) & \mathscr{k}(x_2,x_2) & \mathscr{k}(x_2,x_3) & \cdots & \mathscr{k}(x_2,x_n) \\ \vdots & \vdots & \vdots & \ddots & \vdots \\ \mathscr{k}(x_n,x_1) & \mathscr{k}(x_n,x_2) & \mathscr{k}(x_n,x_3) & \cdots & \mathscr{k}(x_n,x_n) \end{bmatrix}. \tag{23}$$

y conditioned distribution on $\mathscr{G}$ is represented by $p(y|\mathscr{G},x_i)=N(\mathscr{G},\sigma_n^2 I)$. Here, I is the unit matrix of n dimensions.

To estimate the eventual quantity y_* and its covariance $\mathrm{cov}(\mathscr{G}_*)$ for a new input X_*, the joint distribution of y and $\mathscr{G}_*$ is shown as follows:

$$\begin{bmatrix} y \\ \mathscr{G}_* \end{bmatrix}\sim N\left(\begin{bmatrix} 0 \\ 0 \end{bmatrix},\begin{bmatrix} \mathscr{K}(X,X)+\sigma^2 I & \mathscr{K}(X,X_*) \\ \mathscr{K}(X_*,X) & \mathscr{K}(X_*,X_*) \end{bmatrix}\right), \tag{24}$$

where $\mathscr{K}(X,X)$ and $\mathscr{K}(X_*,X_*)$ denote the training and checking data phases of a covariance $(n\times 1)$ matrix of test samples X_*, respectively.

The conventional method for conditioning Gaussian is used to generate the predictive distribution and is defined as follows:

$$p(\mathscr{G}_*|X,y,X_*)\sim N\left(\overline{\mathscr{G}_*},\mathrm{cov}(\mathscr{G}_*)\right), \tag{25}$$

where $\overline{\mathscr{G}_*}=\mathscr{K}(X_*,X)[\mathscr{K}(X,X)+\sigma^2 I]^{-1}\mathscr{G}$, $\mathrm{cov}(\overline{\mathscr{G}_*})=\mathscr{K}(X_*,X_*)-\mathscr{K}(X_*,X)[\mathscr{K}(X,X)+\sigma^2 I]^{-1}\mathscr{K}(X,X_*)$.

3.2.2. Kernel Functions. A kernel (or covariance function) describes the covariance $\mathrm{cov}(\mathscr{G}_*)$ of the GPR variables. Kernel function calculates the closeness and similarity degree among the actual datasets. Therefore, it determines the analyses of GPR in handling systematic prediction error.

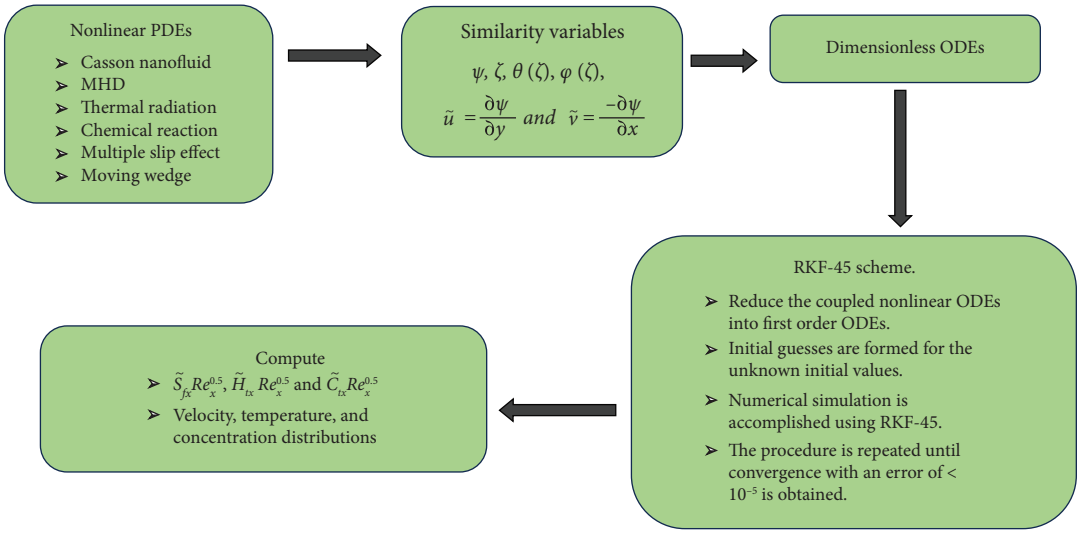

Figure 2: Flowchart procedure of RKF-45.

Table 1: Comparison of values for $\tilde{S}_{fx} Re_x^{0.5}$ for various values of m.

m	Ishak et al. [36]	Ullah et al. [37]	Current outcome
0	0.4696	0.4696	0.4696
0.0141	0.5046	0.5046	0.5046
0.0435	0.5690	0.5690	0.5690
0.0909	0.6550	0.6550	0.6550
0.1429	0.7320	0.7320	0.7320
0.2000	0.8021	0.8021	0.8021
0.3333	0.9277	0.9277	0.9277
0.5000	—	—	—
1	1.2326	1.2326	1.2326
5	1.5504	1.5505	1.5505
100	1.6794	1.6794	1.6794
∞	1.6872	1.6872	1.6872

Table 2: Comparison of values for $\tilde{H}_{tx} Re_x^{0.5}$ for various values of Pr.

Pr	Kuo [38]	Raju and Sandeep [16]	Current outcome
1000	4.7901	4.7901	4.7901
100	2.2229	2.2229	2.2229
30	1.4873	1.4873	1.4873
10	1.02974	1.02974	1.0297
1	0.46960	0.46960	0.4696
0.72	0.41809	0.41786	0.4181

There are several types of Kernel functions that can be used in GPR. For example, exponential (E), squared exponential (SE), rational quadratic (RQ), Matérn class (MT), ardexponential (ardE), ardsquared exponential (ardSE), and ardrational quadratic (ardRQ), which are defined as follows:

$$\begin{aligned}
\mathscr{K}_{Ex}\left(X, X'\right) &= \sigma^2 \exp\left(-\frac{\left\|X - X'\right\|}{2L^2}\right),\\
\mathscr{K}_{SE}\left(X, X'\right) &= \sigma^2 \exp\left(-\frac{\left\|X - X'\right\|^2}{2L^2}\right),\\
\mathscr{K}\left(X, X'\right) &= 1 + \left(\frac{\left\|X - X'\right\|^2}{\left\|X - X'\right\|^2 + \mathfrak{c}}\right),\\
\mathscr{K}_{Ma}\left(X, X'\right) &= \frac{2^{1-\xi}}{\Gamma(\xi)}\left(\sqrt{2\xi}\ \frac{\left\|X - X'\right\|}{L}\right)^{\varsigma} \mathscr{K}_{\varsigma}\left(\sqrt{2\xi}\ \frac{\left\|X - X'\right\|}{L}\right)^{\varsigma},
\end{aligned} \tag{26}$$

where $\sigma, L, \mathfrak{c}, \xi, \Gamma$, and $\mathscr{K}_{\varsigma}$ indicate the standard deviation, parameter of length scale, the signal, intercept constant, smooth factor, Gamma, and Bessel function, respectively.

4. Results and Discussion

In this section, the important features of the flow, heat transfer, and mass transfer are achieved using Casson fluid flow over a moving wedge with slip effects and also the GPR technique was developed to predict the skin friction coefficient ($\widetilde{S}_{fx}$), heat transfer rate ($\widetilde{H}_{tx}$), and nanoparticle transfer rate ($\widetilde{C}_{tx}$).

4.1. Analysis of Physical Quantities. This section visualizes the physical description of engaged parameters developing in equations (12)–(16). The sixteen distinct nondimensional parameters, such as $m, M, \gamma, \beta, S, K, \delta, R_d, \Pr, Ec, Nb, Nt, Bi_1, Bi_2, Le$, and R, and the corresponding ranges of constraints of the research are exhibited in Table 3. The numerical illustration for $\widetilde{S}_{fx}Re_x^{0.5}, \widetilde{H}_{tx}\ Re_x^{0.5}$, and $\widetilde{C}_{tx}Re_x^{0.5}$ is shown in Tables 4–6. A prominent variation in $\widetilde{S}_{fx}Re_x^{0.5}$ has been noticed for β and S. However, $\widetilde{H}_{tx}\ Re_x^{0.5}$ is enhanced for more tremendous values of R_d, Ec, Nb, Nt, whereas $\widetilde{C}_{tx}Re_x^{0.5}$ decreases with Nb, Le, R, and Bi_2 and increases with Nt and Bi_2.

4.2. Discussion of Results

4.2.1. Velocity Distribution. Figure 3 presents the significant impact of β and m on $f'(\zeta)$. Decreasing completion is perceived in $f'(\zeta)$ for greater values of β. Because they inversely correlate to the yield stress and fluid viscosity rate, the velocity field $f'(\zeta)$ declines as β upturns. Viscous force, a resistive force, is created and is what causes this distortion. This force's energy grows as the Casson nanofluid parameter's strength is enhanced with a decrease in the surface's thickness in response to fluid movement within the boundary layer. The velocity field $f'(\zeta)$ tends to improve when Hartree pressure gradient m credits are enhanced because they exert an intensity force on the flow and also inverse variation is performed between m and the velocity boundary layer thickness. Figure 4 reflects the effect of S and M on $f'(\zeta)$. A raised velocity distribution is examined with unsteadiness parameter. It provides that the velocity boundary layer thickness imperceptibly increases with an increment in S. Also, the broadening magnetic parameter is taking over the force to dwindle the velocity component. Physically, this occurs due to the fact that by boosting the values of M, the Lorentz force diminishes, which leads to the retarding force on the movement of the fluid. Figure 5 shows the effects of K and γ on $f'(\zeta)$. In both cases, a widening of the momentum boundary layer is inspected. As is evident, the greatest levels of γ cause greater force on the flow of the velocity field $f'(\zeta)$. The influence of δ on $f'(\zeta)$ is depicted in Figure 6. With an increase of δ, the velocity distribution grows up. Therefore, the slip at the wedge surface energetically leads to the closeness of the boundary layer.

4.2.2. Temperature Distribution. To examine the variation in $\theta(\zeta)$ against various flow parameters, Figures 7–13 are developed. From Figures 7 and 8, it is noticed that the increasing values of β and M result in an augmentation of both the rate of heat transfer and the temperature profile. It can be attributed to alterations in the fluid's rheological properties, flow dynamics, and the influence of the magnetic field. These changes collectively impact the thermal behavior of the system, leading to enhanced heat transfer and temperature profiles. A reverse phenomenon is perceived for growing values of m and S on $\theta(\zeta)$. Figures 9 and 10 point out that upon increasing K, γ, and δ, the decline is made in the heat transfer rate and $\theta(\zeta)$. Enhancing Ec strengthened the internal energy of nanoliquid which in turn augmented the

Table 3: Nondimensional parameters on the physical features.

SI. no.	Nondimensional parameters	Range
1	Hartree pressure gradient parameter (m)	0.1–0.5
2	Magnetic parameter (M)	0.0–1.5
3	Casson fluid parameter (β)	0.1–1.0
4	Unsteadiness parameter (S)	0.0–0.4
5	Porosity parameter (K)	0.0–1.0
6	Moving wedge parameter (γ)	−0.5–0.5
7	Radiation parameter (R_d)	0.0–2.5
8	Prandtl number (Pr)	1.0–10.0
9	Eckert number (Ec)	0.0–1.0
10	Brownian motion parameter (Nb)	0.3–2.0
11	Thermophoresis parameter (Nt)	0.2–2.0
12	Lewis number (Le)	1.0–3.0
13	Slip parameter (δ)	0.0–2.0
14	Biot number (Bi_1)	0.5–5.0
15	Biot number (Bi_2)	0.5–2.0
16	Chemical reaction parameter (R) ($R > 0$ corresponds to calamitous chemical reaction $R <$ (progressive chemical reaction)	−0.5–0.5

Table 4: Numerical outcome of skin friction coefficient ($\widetilde{S}_{fx} Re_x^{0.5}$).

β	m	S	M	K	γ	δ	$\widetilde{S}_{fx} Re_x^{0.5}$
0.1							0.2762
0.3							0.4361
1							0.5587
	0.1						0.5074
	0.3						0.5204
	0.5						0.5258
		0.1					0.5038
		0.2					0.5152
		0.3					0.5262
			0.5				0.5152
			1.0				0.4210
			1.5				0.2544
				0.2			0.4131
				0.4			0.5152
				0.6			0.5868
					−0.5		0.9085
					0.2		0.5152
					0.5		0.3293
						0.5	0.3728
						1.0	0.2533
						1.5	0.1913

Table 5: Numerical outcome of heat transfer rate ($\widetilde{H}_{tx}\, Re_x^{0.5}$).

Pr	R_d	Ec	Nb	Nt	$\widetilde{H}_{tx}\, Re_x^{0.5}$
1					−0.3099
3					−0.3615
5					−0.3920
	0.5				−0.3099
	1.0				−0.2910
	1.5				−0.2763
		0.4			−0.2922
		0.8			−0.2567
		1.0			−0.2389

Table 5: Continued.

Pr	R_d	Ec	Nb	Nt	$\widetilde{H}_{tx}\, Re_x^{0.5}$
			0.5		−0.3066
			1.0		−0.2982
			1.5		−0.2898
				1.0	−0.2953
				1.5	−0.2863
				2.0	−0.2775

Table 6: Numerical outcome of nanoparticle transfer rate ($\widetilde{C}_{tx}Re_x^{0.5}$).

Nb	Nt	Le	R	Bi_1	Bi_2	$\widetilde{C}_{tx}Re_x^{0.5}$
1.0						−0.4596
1.5						−0.4617
2.0						−0.4627
	0.5					−0.4211
	1.0					−0.3934
	1.5					−0.3793
		1.5				−0.4269
		2.0				−0.4448
		2.5				−0.4580
			−0.5			−0.1218
			0.2			−0.4215
			0.5			−0.4539
				1.0		−0.4368
				2.0		−0.4307
				3.0		−0.4281
					0.5	−0.4448
					1.0	−0.6960
					1.5	−0.9698

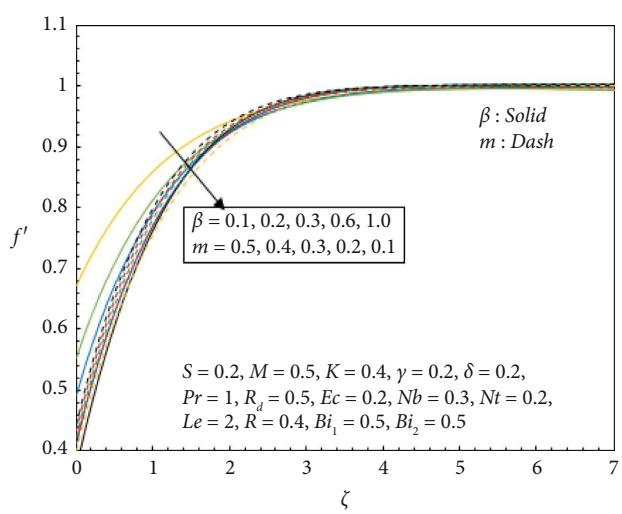

Figure 3: Impact of β and m on $f'(\zeta)$.

heat transfer rate. Physically, the ?? is employed to simulate a relationship between the boundary layer enthalpy difference and kinetic energy. A liquid is only warmed internally by friction between its particles when a wedge expands, converting mechanical energy to thermal energy. The enhancement in Ec at the wedge surface raises the thermal energy associated with fluid motion by raising the temperature of the fluid and producing a thicker boundary layer. The response of $\theta(\zeta)$ to the variation of Prand R_d is illustrated in Figure 11. The detected results show that the amount of $\theta(\zeta)$ is impeded for greater values of Pr. When Pr increases, the momentum diffusivity outweighs the thermal

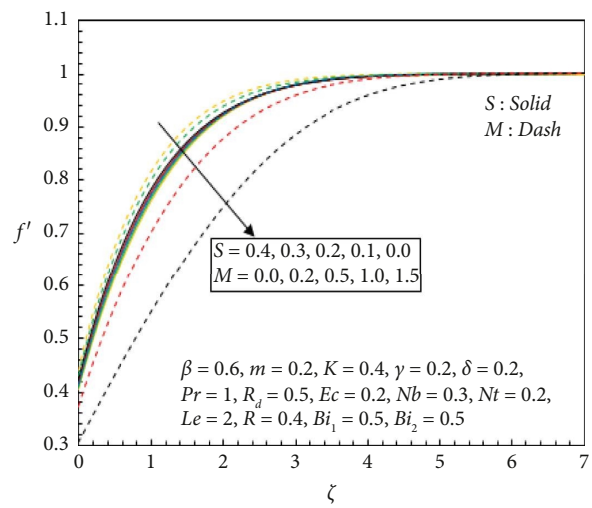

Figure 4: Impact of S and M on $f^{'}(\zeta)$.

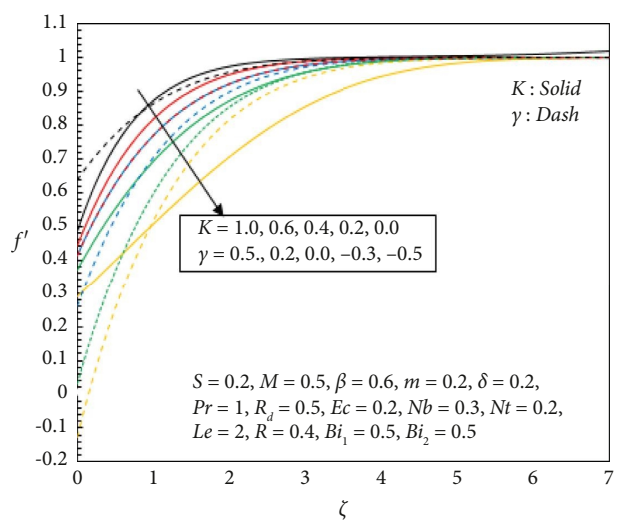

Figure 5: Impact of K and γ on $f^{'}(\zeta)$.

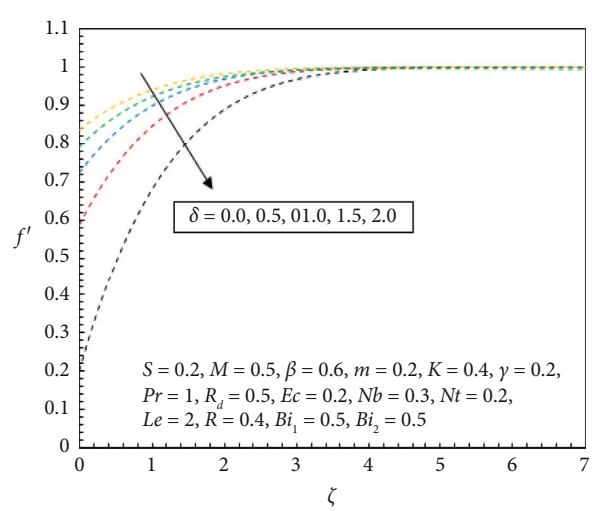

Figure 6: Impact of δ on $f^{'}(\zeta)$.

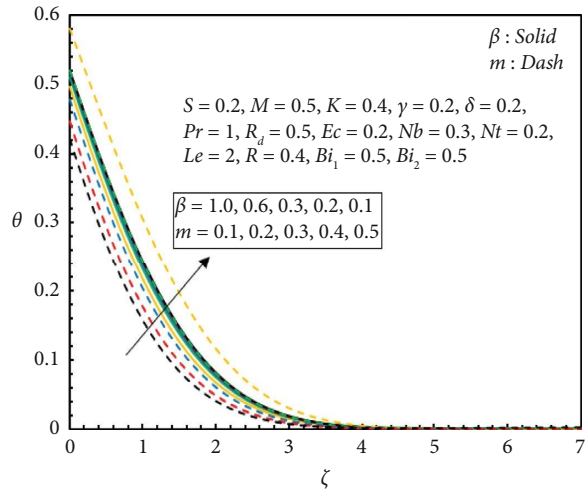

Figure 7: Impact of β and m on $\theta(\zeta)$.

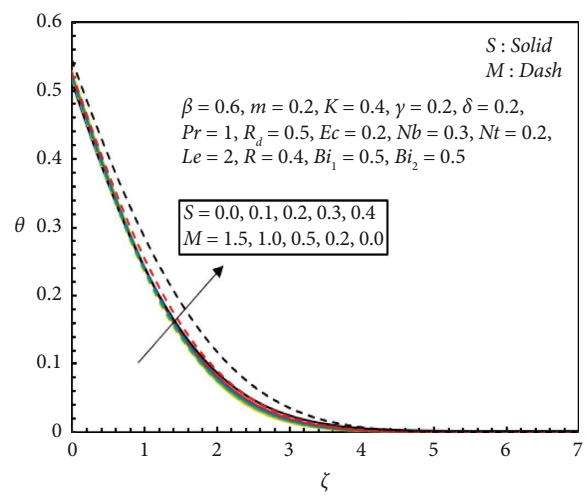

Figure 8: Impact of S and M on $\theta(\zeta)$.

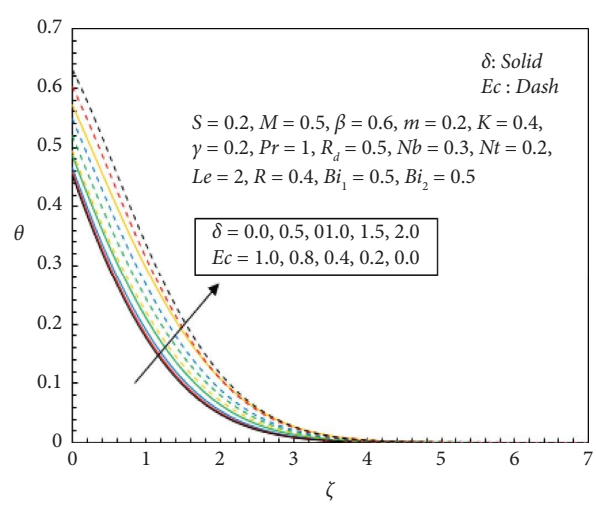

Figure 9: Impact of δ and Ec on $\theta(\zeta)$.

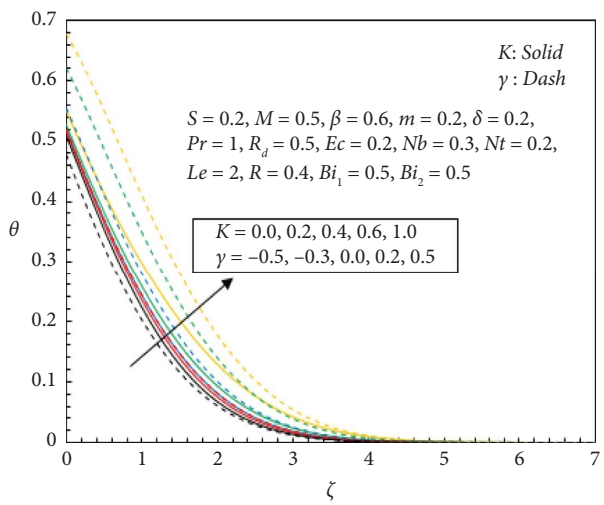

Figure 10: Impact of K and γ on $\theta(\zeta)$.

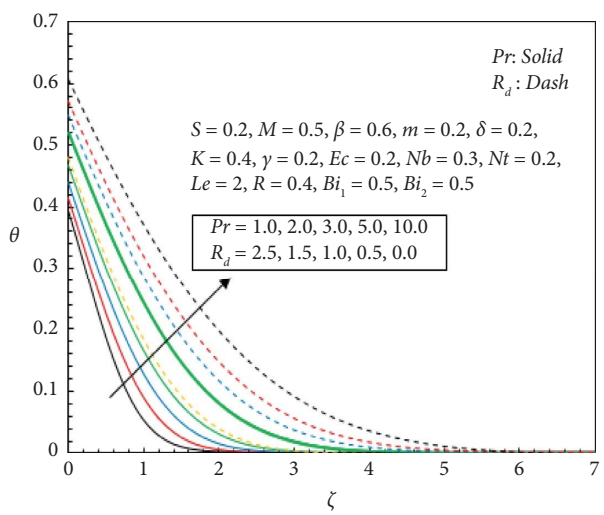

Figure 11: Impact of Pr and R_d on $\theta(\zeta)$.

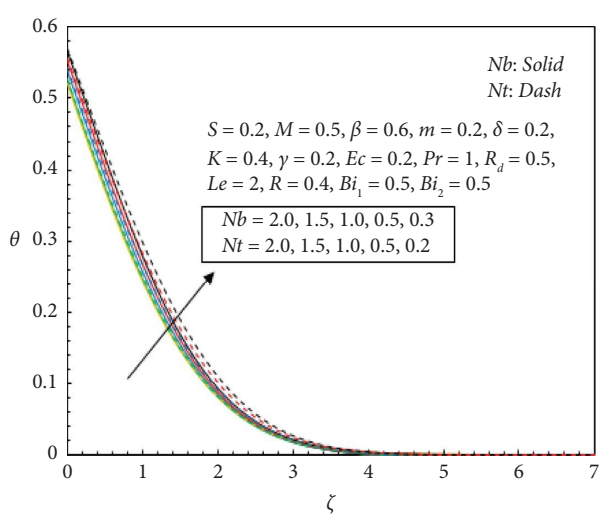

Figure 12: Impact of Nb and Nt on $\theta(\zeta)$.

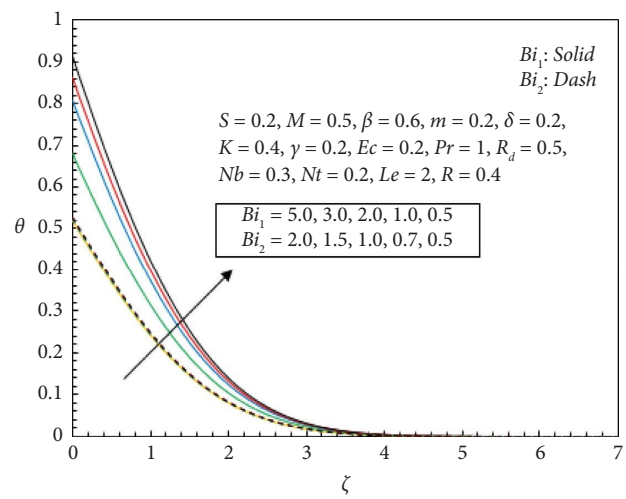

Figure 13: Impact of Bi_1 and Bi_2 on $\theta(\zeta)$.

diffusivity, resulting in a decrease in the flow region's temperature field $\theta(\zeta)$. Augmentation performance is perceived in $\theta(\zeta)$ for higher values of R_d, since increasing R_d spawns more heat which in turn boosts the fluid temperature. Figure 12 witnesses that increasing Nb increases the kinetic energy of the particles due to the collision; hence, temperature is made immense. An identical configuration is perceived for cultivating values Nt. From Figure 13, the observations reveal that $\theta(\zeta)$ is larger with the increasing values of Bi_1 and Bi_2. Thermal Biot numbers play an important portrayal in the enhancement of nanoparticles temperature, as it is directly associated with the coefficient of heat transfer.

4.2.3. Concentration Distribution. The influence of peculiar flow parameters such as $\beta, m, M, S, \delta, Ec, K, \gamma, R_d, Nb, Nt, Bi_1, Bi_2, Le$, and R on the concentration of nanoparticles field $\varphi(\zeta)$ is highlighted in Figures 14–21. Figures 14–18 elucidates the increasing nature in $\varphi(\zeta)$ due to increasing values of β, M, and Pr. Inverse variations are seen for the growing values of $m, S, \delta, Ec, K, \gamma$, and R_d. Figure 19 shows the behavior of Nb and Nt on $\varphi(\zeta)$. The increasing value of Nb reduces $\varphi(\zeta)$, and this is due to the fact that Brownian motion makes the fluid mild within the frontier and the absence of particle removal from the fluid regime to the surface results in a reduction in $\varphi(\zeta)$ while increasing (Nt) augmented $\varphi(\zeta)$. Boosting (Nt) enhances the motion of nanoparticles from higher to lower temperature gradient which in turn exploits the concentration of nanoparticles. Figure 20 illustrates the behavior on $\varphi(\zeta)$ for signified Bi_1 and Bi_2. It is discerned that $\varphi(\zeta)$ is improved for greater evaluation of Bi_1 and Bi_2. Because the Biot numbers of nanoparticle concentration are directly correlated with the coefficient of mass transfer, they play a significant role in the enhancement of nanoparticle concentration. Figure 21 demonstrates the influence of Le and R on $\varphi(\zeta)$. It is depicted that the improving credits of Le cause a decline in $\varphi(\zeta)$ because Le has an inverse relationship with the

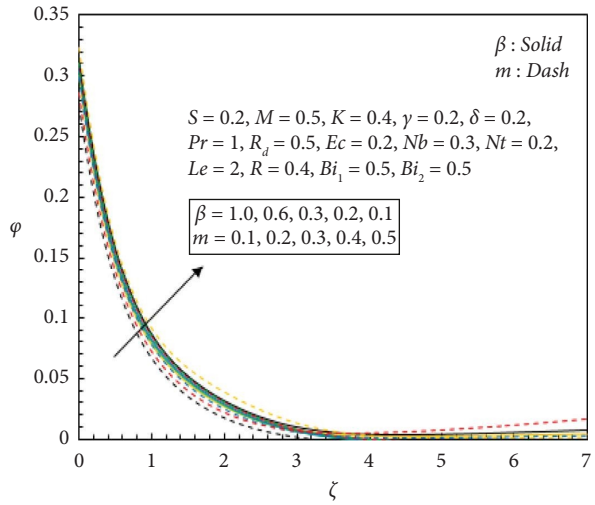

Figure 14: Impact of β and m on $\varphi(\zeta)$.

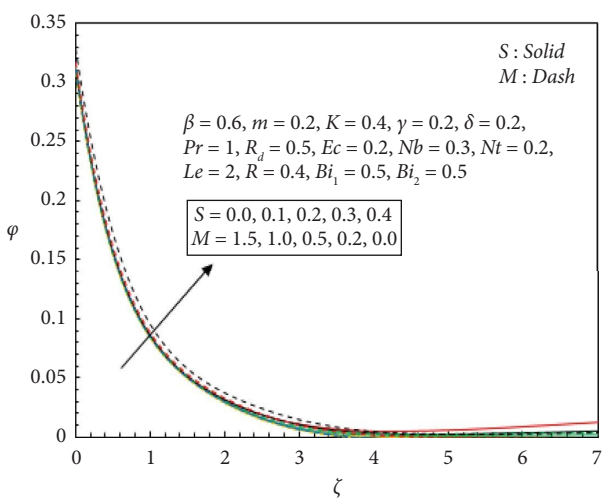

Figure 15: Impact of S and M on $\varphi(\zeta)$.

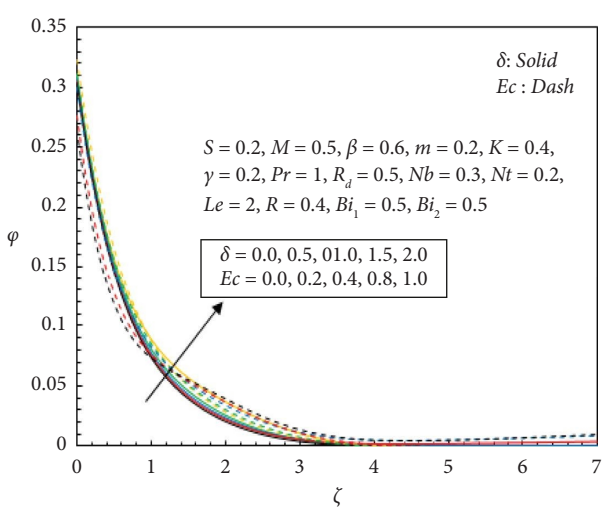

Figure 16: Impact of δ and Ec on $\varphi(\zeta)$.

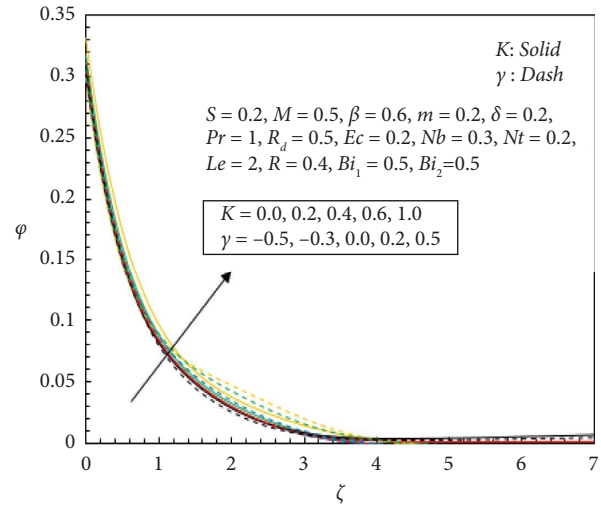

Figure 17: Impact of K and γ on $\varphi(\zeta)$.

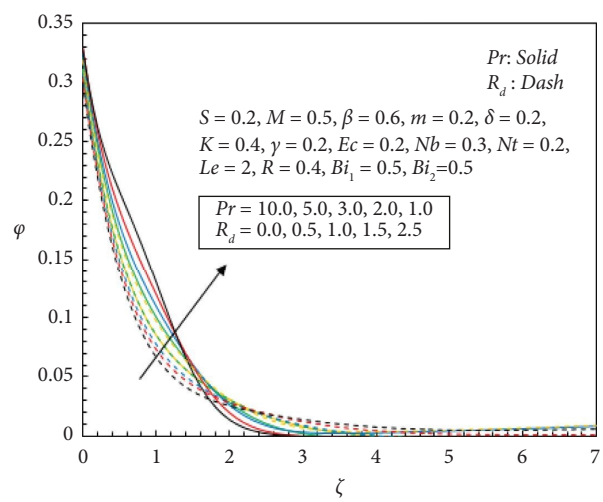

Figure 18: Impact of Pr and R_d on $\varphi(\zeta)$.

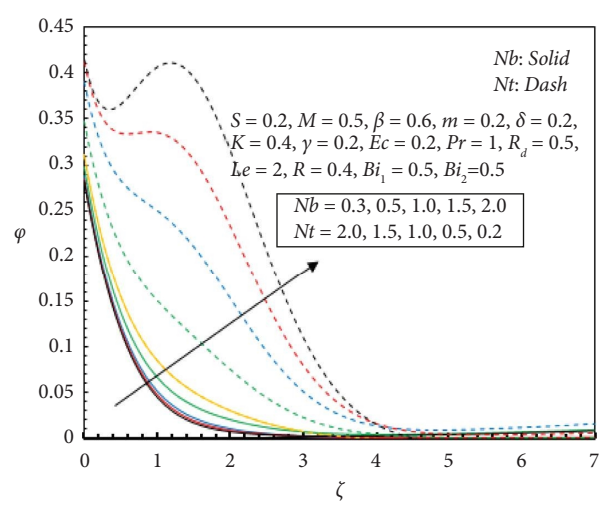

Figure 19: Impact of Nb and Nt on $\varphi(\zeta)$.

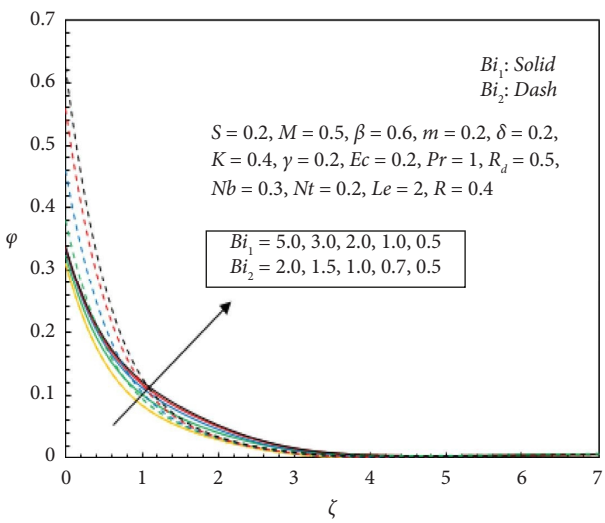

Figure 20: Impact of Bi_1 and Bi_2 on $\varphi(\zeta)$.

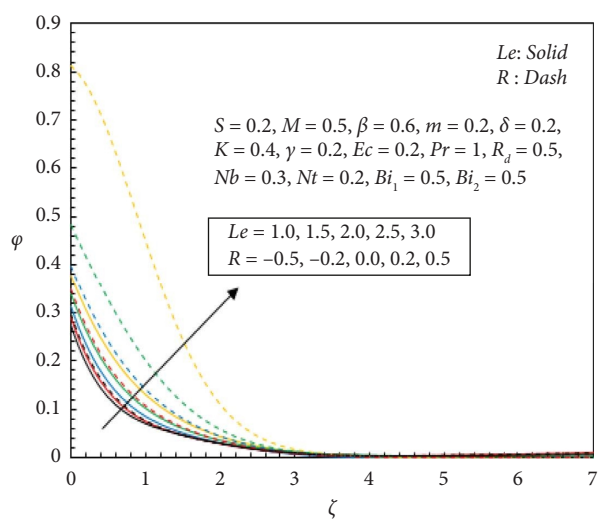

Figure 21: Impact of Le and R on $\varphi(\zeta)$.

Brownian dispersion factor. As Le grows, a Brownian factor of dispersion falls, resulting in a reduction in nanoparticle concentration $\varphi(\zeta)$ and boundary layer thickness. Also, boosting R influences $\varphi(\zeta)$, which in turn affects mass transport rates, chemical rates, and nanoparticle concentrations, and subsequently, temperature and humidity fields. The consequences include detrimental effects on yields, such as freezing damage, and a shift in energy distribution towards a rainy cooling tower.

4.3. Mathematical Model Using GPR. In this section, we proposed a novel data-driven model based on Gaussian process regression (GPR) technique to predict $\widetilde{S}_{fx}Re_x^{0.5}$, $\widetilde{H}_{tx}\,Re_x^{0.5}$, and $\widetilde{C}_{tx}Re_x^{0.5}$ based on numerical output. This model is more flexible and can handle uncertainty in data. GPR is rooted in a Bayesian framework, which allows for the incorporation of prior knowledge or domain expertise into the model. This can improve its performance,

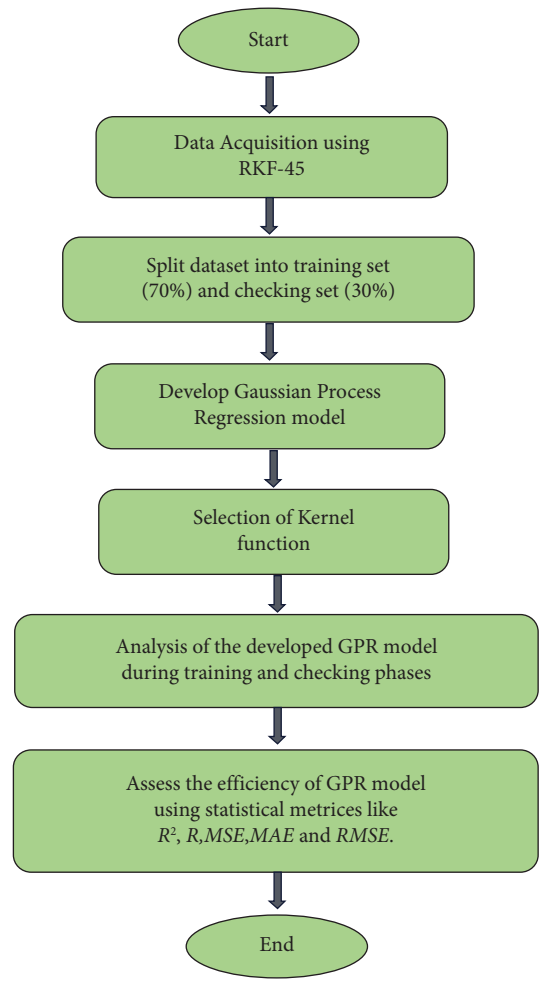

Figure 22: Workflow diagram for the GPR model.

especially when we have relevant prior information. In the present study, the developed GPR model uses $m, M, \gamma, \beta, S, K, \delta, R_d, \Pr, Ec, Nb, Nt, Bi_1, Bi_2, Le,$ and R as the input parameters. The data have been collected from the numerical results using RKF-45. Here, 70% of the dataset is used in the training phase and 30% is used in the checking phase. Figure 22 gives the workflow of the proposed GPR model for estimating the skin friction coefficient ($\widetilde{S}_{fx}$), heat transfer rate ($\widetilde{H}_{tx}$), and nanoparticle transfer ($\widetilde{C}_{tx}$).

GPR model depends on the choice of kernel function and hyperparameters, which should be carefully selected through cross-validation and grid search. This practice helps avoid overfitting, where the model performs well on the training data but fails to generalize to new, unseen data. Table 7 represents the prediction error of the developed GPR model for different kernel functions. The lower error levels and the highest R^2 indicate a superior model. From Table 7, we noticed that the exponential Kernel function has better prediction of $\widetilde{S}_{fx}Re_x^{0.5}$, $\widetilde{H}_{tx}\,Re_x^{0.5}$, and $\widetilde{C}_{tx}Re_x^{0.5}$ results for both training and checking phases of magnetized Casson nanofluid. Also, the determined R^2 values for the exponential kernel function have better performance than other functions in both training and checking phases.

Table 7: Prediction errors of the GPR model with different kernel functions.

Physical quantities	Statistical metrics	GPR training phase				GPR checking phase			
		Kernel functions							
		Exponential	Squared exponential	Rational quadratic	Matérn	Exponential	Squared exponential	Rational quadratic	Matérn
$\widetilde{S}_{fx}Re_x^{0.5}$	MSE	**2.04E − 10**	1.37E − 08	1.43E − 08	1.72E − 08	**1.67E − 09**	1.42E − 05	1.36E − 05	1.98E − 07
	MAE	**8.34E − 06**	5.78E − 05	5.06E − 05	5.73E − 05	**3.09E − 05**	2.94E − 03	2.82E − 03	0.000321
	MAPE	**2.54E − 03**	1.48E − 02	1.47E − 02	1.55E − 02	**7.25E − 03**	6.13E − 01	5.84E − 01	0.069743
	MAPE	**1.43E − 05**	0.000117	0.000119	0.000131	**4.09E − 05**	0.003764	0.003689	0.000445
	R^2	**0.999999982**	0.999998799	0.999998718	0.99999451	**0.999999973**	0.999774302	0.999783212	0.999996841
	R	**0.99999991**	0.00000383	0.999999359	0.999999226	**0.999999987**	0.999887145	0.9998916	0.999998421
$\widetilde{H}_{tx}\,Re_x^{0.5}$	MSE	**2.72E − 09**	9.27E − 06	6.56E − 08	7.55E − 08	**2.28E − 10**	1.40E − 08	1.22E − 08	7.72E − 09
	MAE	**2.95E − 05**	1.96E − 03	1.36E − 04	1.55E − 04	**8.87E − 06**	7.09E − 05	6.97E − 05	5.09E − 05
	MAPE	**1.02E − 02**	6.59E − 01	4.49E − 02	5.12E − 02	**2.65E − 03**	2.31E − 02	2.23E − 02	0.0152
	RMSE	**5.22E − 05**	0.003045	0.000256	0.000275	**1.51E − 05**	0.000118	0.000111	8.79E − 05
	R^2	**0.999997263**	0.9906798	0.999934081	0.999924121	**0.999999974**	0.999998392	0.999998589	0.999999111
	R	**0.999998632**	0.995328991	0.99996704	0.99996206	**0.999999987**	0.999999196	0.999999295	0.999999555
$\widetilde{C}_{tx}Re_x^{0.5}$	MSE	**1.51E − 08**	2.76E − 07	2.76E − 07	2.27E − 07	**5.60E − 10**	6.67E − 05	1.14E − 07	7.26E − 08
	MAE	**6.45E − 05**	3.36E − 04	3.36E − 04	2.99E − 04	**1.31E − 05**	5.24E − 03	1.64E − 04	0.00012481
	MAPE	**1.46E − 02**	7.52E − 02	7.52E − 02	6.69E − 02	**4.91E − 03**	1.64E + 00	4.76E − 02	0.039045
	RMSE	**1.23E − 04**	0.000526	0.000526	0.000476	**2.37E − 05**	0.008165	0.000337	0.000269
	R^2	**0.999822566**	0.996755364	0.996755366	0.997335641	**0.99999998**	0.997567793	0.999995848	0.999997353
	R	**0.999911279**	0.998376364	0.998376365	0.998666932	**0.99999999**	0.998783156	0.999997924	0.999998677

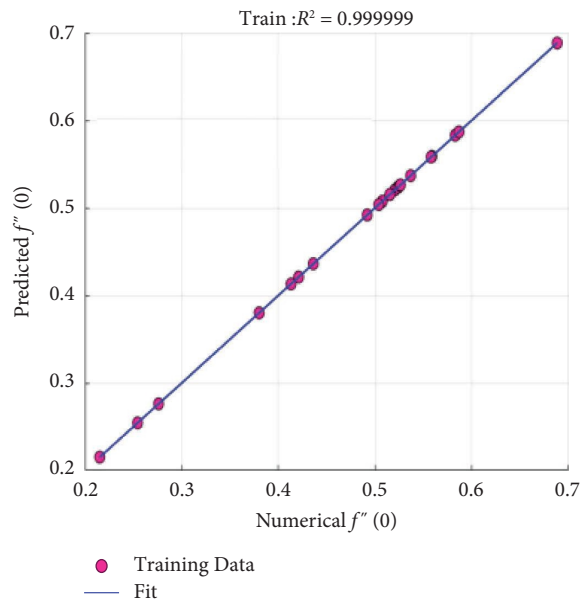

Figure 23: Predicted vs. numerical values of training $f''(0)$ dataset.

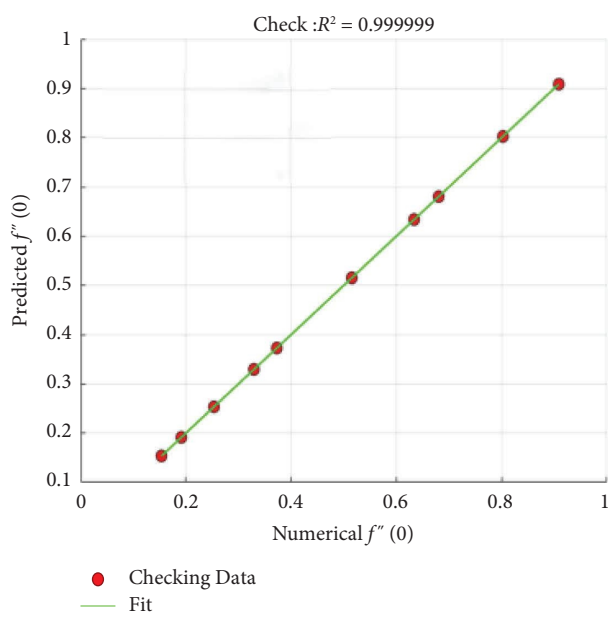

Figure 24: Predicted vs. numerical values of checking $f''(0)$ dataset.

4.3.1. Performance Assessment. Evaluating the model's performance using various statistical metrics is a standard practice in machine learning and regression analysis. Hence, the performance assessment of error between the GPR model and the numerical data of magnetized Casson nanofluid was employed and compared using statistical metrics including root mean square error (RMSE), mean absolute error (MAE), mean absolute percentage error

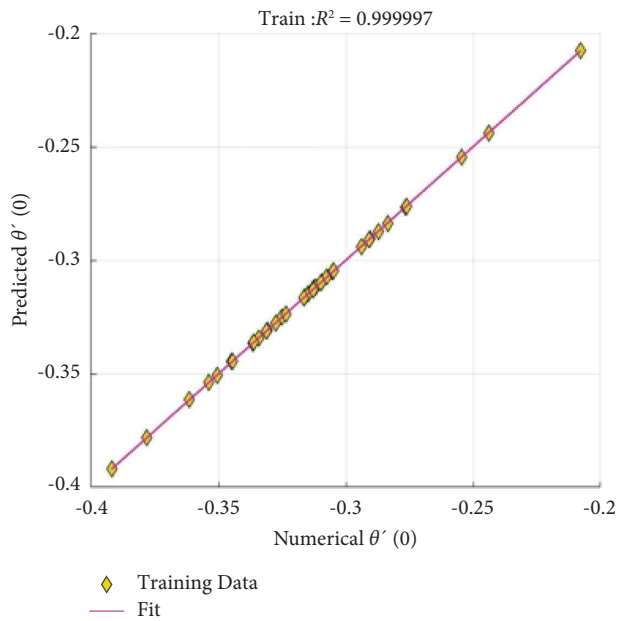

Figure 25: Predicted vs. numerical values of training θ' (0) dataset.

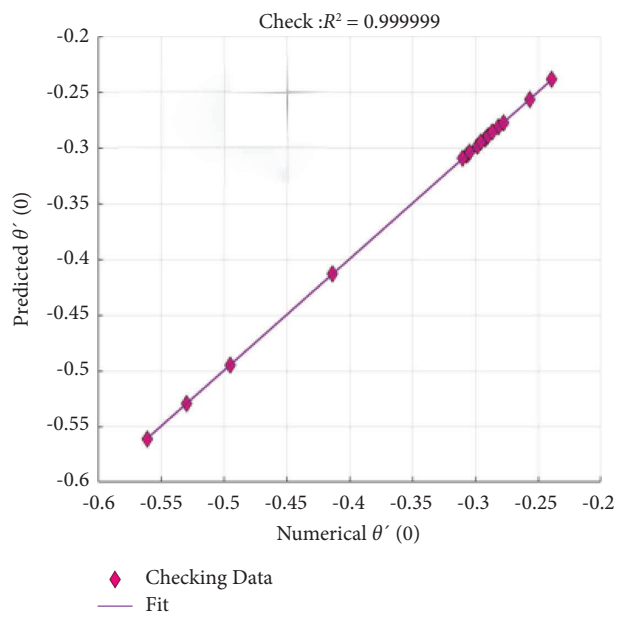

Figure 26: Predicted vs. numerical values of checking θ' (0) dataset.

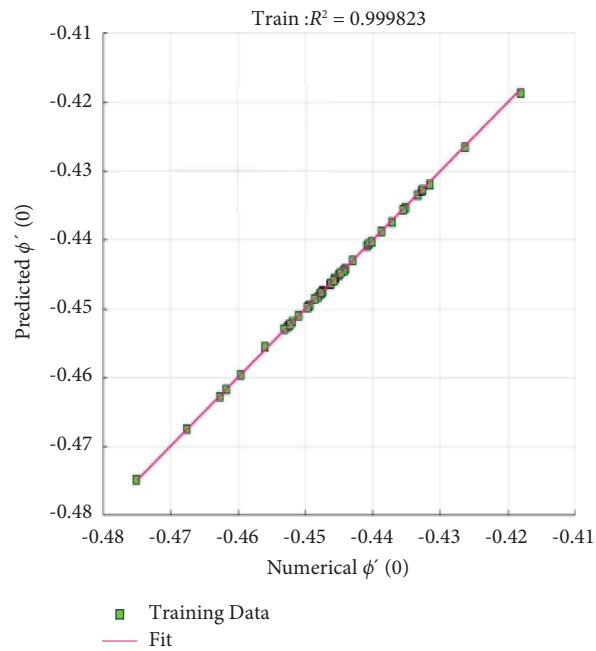

Figure 27: Predicted vs. numerical values of training $\phi'(0)$ dataset.

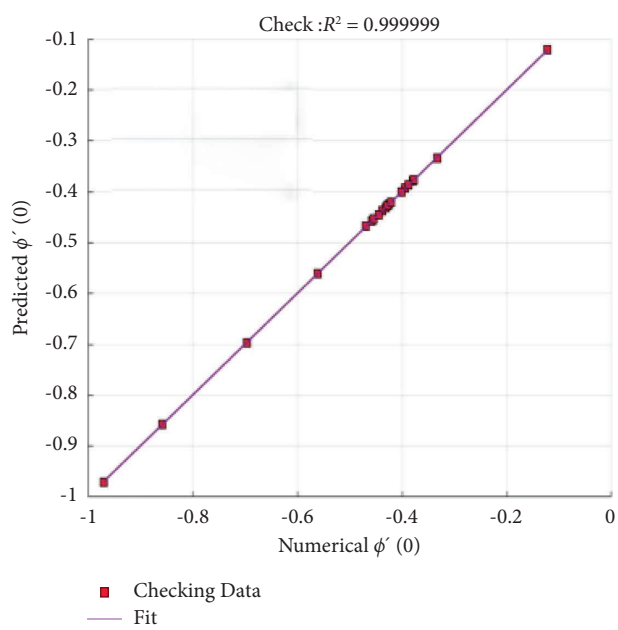

Figure 28: Predicted vs. numerical values of checking $\phi'(0)$ dataset.

(MAPE), mean square error (MSE), coefficient of determination (R^2), and correlation coefficient (R). The mentioned metrics are defined as follows:

$$\begin{aligned}
\mathrm{RMSE} &= \sqrt{\frac{1}{n_{ds}}\sum_{i=1}^{n_{ds}}\left(y_i^{\mathrm{numerical}} - y_i^{\mathrm{predicted}}\right)^2},\\
\mathrm{MAE} &= \frac{1}{n_{ds}}\sum_{i=1}^{n_{ds}}\left|y_i^{\mathrm{numerical}} - y_i^{\mathrm{predicted}}\right|,\\
\mathrm{MAPE} &= \frac{1}{n_{ds}}\sum_{i=1}^{n}\left|\frac{y_i^{\mathrm{numerical}} - y_i^{\mathrm{predicted}}}{y_i^{\mathrm{predicted}}}\right|,\\
\mathrm{MSE} &= \frac{1}{n_{ds}}\sum_{i=1}^{n}\left(y_i^{\mathrm{numerical}} - y_i^{\mathrm{predicted}}\right)^2,\\
R^2-\mathrm{score} &= 1-\frac{\sum_{i=1}^{n_{ds}}\left(y_i^{\mathrm{numerical}} - y_i^{\mathrm{predicted}}\right)^2}{\sum_{i=1}^{n_{ds}}\left(y_i^{\mathrm{numerical}} - \mu\right)^2},\\
R-\mathrm{score} &= \frac{\sum_{i=1}^{n_{ds}}\left(y_i^{\mathrm{numerical}} - \overline{y_i}\right)\left(\overline{y_i^{\mathrm{numerical}}} - \overline{y_i^{\mathrm{predicted}}}\right)}{\sqrt{\sum_{\mathfrak{K}=1}^{\mathfrak{n}_{ds}}\left(y_i^{\mathrm{numerical}} - \overline{y_i}\right)}\sqrt{\sum_{\mathfrak{K}=1}^{\mathfrak{n}_{ds}}\left(\overline{y_i^{\mathrm{numerical}}} - \overline{y_i^{\mathrm{predicted}}}\right)}},
\end{aligned} \tag{27}$$

where n_{ds}, $y_i^{\mathrm{numerical}}$, $y_i^{\mathrm{predicted}}$, μ, $\overline{y_i^{\mathrm{numerical}}}$, and $\overline{y_i^{\mathrm{predicted}}}$ indicate the number of datasets, the target value, the predicted value, the measured average and mean of targeted and predicted values, respectively.

4.3.2. GPR Model Validation with Numerical Simulation. For better judgement about the developed GPR model, the simultaneous demonstration of numerical and predicted results of $\widetilde{S}_{fx}Re_x^{0.5}$, $\widetilde{H}_{tx}\,Re_x^{0.5}$, and $\widetilde{C}_{tx}Re_x^{0.5}$ is depicted in Figures 23–28. The symmetrical straight lines are targeted values from these figures, and the predicted values are represented near and far away from the straight lines. In all the figures, the numerical and measured values of $f''(0)$, $\theta'(0)$, and $\phi'(0)$ for training and checking phases showed superior predictive performance. The R^2 values taped for training and checking phases of $f''(0)$ are 0.999999 and 0.999999, of $\theta'(0)$ are 0.99997 and 0.999999, and of $\phi'(0)$ are 0.999823 and 0.999999, respectively. These figures state the high accuracy prediction of engineering physical interest quantities of magnetized Casson nanofluid using GPR models.

5. Conclusions

The flow behavior of magnetized Casson nanofluid over a wedge subject to multiple slip effects, thermal radiation, and chemical reaction was addressed and discussed in detail. The RKF-45 together with the shooting technique was utilized to simulate the numerical steady similarity solutions. The computational outcomes are obtained through the GPR (Gaussian process regression) intelligent soft computing technique for estimating the dynamic behavior of Casson nanofluid models. The computations are shown as follows:

(i) From the mathematical simulation, the addition of β and M devaluates the momentum boundary layer thickness.

(ii) The distribution of velocity attains maximum for higher values of K, γ, and δ.

(iii) The nanoparticle temperature enhances with the increase of R_d, Ec, Nb, Nt, Bi_1, and Bi_2.

(iv) As Le increases, both the nanoparticle temperature and concentration decrease.

(v) When $R<0$, the nanoparticle concentration rises. Conversely, when $R>0$, the nanoparticle concentration decreases.

(vi) All three employed GPR models have an R^2 value higher than 0.9. An R^2 value of 0.9 indicates a very strong correlation between the predicted and actual values.

(vii) Considering statistical metrics such as RMSE, MAE, MAPE, and MSE, the developed GPR models are more accurate in predicting $\widetilde{S}_{fx}Re_x^{0.5}$, $\widetilde{H}_{tx}\,Re_x^{0.5}$, and $\widetilde{C}_{tx}Re_x^{0.5}$ values.

(viii) This study suggests that the GPR models are effective in simulating and predicting heat and mass transfer coefficients of complex physical flow problems.

Nomenclature

$\tilde{u}_w^*, \tilde{u}_e^*$: Stretching and free stream velocity (m/s)
$\tilde{U}_w^*, \tilde{U}_{fs}^*, \tilde{\varepsilon}$: Positive constants
m: Hartree pressure gradient
$\tilde{B}_0^*$: Magnetic induction parameter (T)
B: Magnetic field
t: Time
$\tilde{T}_w, \tilde{T}_{fs}$: Temperature near and far away from the wedge wall (K)
$\tilde{C}_w, \tilde{C}_{fs}$ C: Concentration near and far away from the wedge surface
D_B, D_T: Brownian and thermophoresis diffusion coefficient (m^2/s)
π: Product of the rate of strain tensor
P_y: Yield stress of the fluid
$\tilde{e}_{ij}^*$: Deformation rate
π_c: Critical value based on Casson non-Newtonian model
T: Temperature (K)
C: Nanoparticle concentration (moles/kg)
N_0, h_0, h_1: Constants
k_c: Rate of chemical reaction (1/s)
$\tilde{u}, \tilde{v}$: Velocity components of x and y directions (m/s)
x: Distance along the surface (m)
y: Distance normal to the surface (m)
f: Dimensionless velocity
M: Magnetic parameter
Pr: Prandtl number
R_d: Radiation parameter
K: Porosity parameter
S: Unsteadiness parameter
R: Chemical reaction parameter
Nb: Brownian motion parameter
Nt: Thermophoresis parameter
Ec: Eckert number
Le: Lewis number
Bi_1, Bi_2: Biot numbers
$\tilde{S}_{fx}$: Skin friction coefficient (Pascal)
$\tilde{H}_{tx}$: Heat transfer rate
$\tilde{C}_{tx}$: Nanoparticle transfer rate
Re_x: Reynolds number
n: Observations
$\mathcal{K}(x, x')$: Covariance or kernel function
L: Parameter of length scale
$\mathfrak{c}$: Signal, intercept constant

Greek Symbols

ζ: Similarity variable
$\tilde{\tau}^*$: Cauchy stress tensor
μ_b: Plastic dynamic viscosity
$\tau = (\rho c)_p/(\rho c)_f$: Ratio of heat capacity of the nanoparticle
ψ: Stream function
σ: Electrical conductivity (S/m)
σ^*: Stefan–Boltzmann constant (W/m^2 K^4)
k^*: Mean absorption coefficient (1/m)
θ: Dimensionless temperature
φ: Dimensionless concentration
γ: Moving wedge parameter
δ: Slip parameter
$\tilde{\Omega}^*$: Total wedge angle
β_1: Wedge angle parameter
β: Casson nanofluid parameter
$\tilde{\tau}_w$: Surface shear stress
q_w: Radiative heat flux
d_w: Radiative mass flux
ϑ: Kinematic viscosity (m^2/s)
ρ: Density (kg/m^3)
c_p: Specific heat
κ: Thermal conductivity (W/m K)
ρc_p: Heat capacity (kg/m^3K)
μ: Dynamic viscosity (kg/m s)
Γ: Gamma function
$\mathcal{K}_\varsigma$: Bessel function
ξ: Smooth factor
ϵ: Gaussian distribution noise value

Subscripts

w: Quantities at wall
fs: Quantities at free stream.

Data Availability

All the data and material used in this research are included in the study.

Conflicts of Interest

The authors declare that they have no conflicts of interest.

References

[1] V. M. Falkner and S. W. Skan, "Some approximate solutions of the boundary layer equations," *Philosophical Magazine*, vol. 12, pp. 865–896, 1931.
[2] I. S. Awaludin, A. Ishak, and I. Pop, "On the stability of MHD boundary layer flow over a stretching/shrinking wedge," *Scientific Reports*, vol. 8, no. 1, Article ID 13622, 2018.
[3] W. Ibrahim and A. Tulu, "Magnetohydrodynamic (MHD) boundary layer flow past a wedge with heat transfer and viscous effects of nanofluid embedded in porous media," *Mathematical Problems in Engineering*, vol. 2019, Article ID 4507852, 12 pages, 2019.
[4] R. B. Kudenatti and H. Amrutha, "MHD boundary layer flow of viscoelastic fluid over a wedge in porous medium," *Archive of Applied Mechanics*, vol. 92, no. 12, pp. 3983–3998, 2022.
[5] E. U. Haq, S. U. Khan, T. Abbas et al., "Numerical aspects of thermo migrated radiative nanofluid flow towards a moving wedge with combined magnetic force and porous medium," *Scientific Reports*, vol. 12, no. 1, Article ID 10120, 2022.
[6] Z. I. Butt, I. Ahmad, M. Shoaib, H. Ilyas, and M. A. Z. Raja, "A novel design of inverse multiquadric radial basis neural networks to analyze MHD nanofluid boundary layer flow past a wedge embedded in a porous medium under the influence of

radiation and viscous effects," *International Communications in Heat and Mass Transfer*, vol. 140, Article ID 106516, 2023.

[7] N. Casson, *A Flow Equation for Pigment-Oil Suspensions of the Printing Ink Type Rheology of Disperse Systems*, Pergamon Press, Oxford, UK, 1951.

[8] A. Hussanan, M. Z. Salleh, I. Khan, and R. M. Tahar, "Heat transfer in magnetohydrodynamic flow of a casson fluid with porous medium and Newtonian heating," *Journal of Nanofluids*, vol. 6, no. 4, pp. 784–793, 2017.

[9] K. A. Khan, A. R. Butt, and N. Raza, "Effects of heat and mass transfer on unsteady boundary layer flow of a chemical reacting Casson fluid," *Results in Physics*, vol. 8, pp. 610–620, 2018.

[10] I. Ullah, I. Khan, and S. Shafie, "Soret and Dufour effects on unsteady mixed convection slip flow of Casson fluid over a nonlinearly stretching sheet with convective boundary condition," *Scientific Reports*, vol. 7, pp. 1113–1119, 2017.

[11] I. Ullah, S. Shafie, I. Khan, and K. L. Hsiao, "Brownian diffusion and thermophoresis mechanisms in Casson fluid over a moving wedge," *Results in Physics*, vol. 9, pp. 183–194, 2018.

[12] S. Guadagni, L. I. Palade, L. Fusi, and A. Farina, "On a Casson fluid motion: nonuniform width symmetric channel and peristaltic Flows," *Fluid*, vol. 6, no. 10, p. 356, 2021.

[13] S. Mukhopadhyay and I. C. Mandal, "Boundary layer flow and heat transfer of a Casson fluid past a symmetric porous wedge with surface heat flux," *Chinese Physics B*, vol. 23, no. 4, Article ID 044702, 2014.

[14] N. T. El-dabe, A. Y. Ghaly, R. R. Rizkallah, K. M. Ewis, and A. S. Al-Bareda, "Numerical solution of MHD boundary layer flow of non-Newtonian casson fluid on a moving wedge with heat and mass transfer and induced magnetic field," *Journal of Applied Mathematics and Physics*, vol. 3, no. 6, pp. 649–663, 2015.

[15] A. Mahdy, "Unsteady MHD slip flow of a non-Newtonian casson fluid due to stretching sheet with suction or blowing effect," *Journal of Applied Fluid Mechanics*, vol. 9, no. 2, pp. 785–793, 2016.

[16] C. S. K. Raju and N. Sandeep, "MHD slip flow of a dissipative Casson fluid over a moving geometry with heat source/sink: a numerical study," *Acta Astronautica*, vol. 133, pp. 436–443, 2017.

[17] P. Ragupathi, S. Saranya, H. V. R. Mittal, and Q. M. Al-Mdallal, "Computational study on three-dimensional convective Casson nanofluid flow past a stretching sheet with Arrhenius activation energy and exponential heat source effects," *Complexity*, vol. 2021, Article ID 5058751, 16 pages, 2021.

[18] P. Ragupathi, T. Muhammad, S. Islam, and A. Wakif, "Application of Arrhenius kinetics on MHD radiative Von Kármán Casson nanofluid flow occurring in a Darcy-Forchheimer porous medium in the presence of an adjustable heat source," *Physica Scripta*, vol. 96, no. 12, Article ID 125228, 2021.

[19] N. Abbas, W. Shatanawi, and K. Abodayeh, "Computational analysis of MHD nonlinear radiation casson hybrid nanofluid flow at vertical stretching sheet," *Symmetry*, vol. 14, no. 7, p. 1494, 2022.

[20] T. A. M. Shatnawi, N. Abbas, and W. Shatanawi, "Comparative study of Casson hybrid nanofluid models with induced magnetic radiative flow over a vertical permeable exponentially stretching sheet," *AIMS Mathematics*, vol. 7, no. 12, pp. 20545–20564, 2022.

[21] S. U. Choi and J. A. Eastman, "Enhancing thermal conductivity of fluids with nanoparticles," *ASME-Publications-FED*, vol. 231, pp. 99–105, 1995.

[22] J. Buongiorno, "Convective transport in nanofluids," *Journal of Heat Transfer*, vol. 128, no. 3, pp. 240–250, 2006.

[23] M. Mustafa, "MHD nanofluid flow over a rotating disk with partial slip effects: Buongiorno model," *International Journal of Heat and Mass Transfer*, vol. 108, pp. 1910–1916, 2017.

[24] V. Makkar, T. Hayat, and A. Alsaedi, "A mathematical simulation of unsteady MHD Casson nanofluid flow subject to the influence of chemical reaction over a stretching surface: Buongiorno's model," *Heat Transfer*, vol. 50, no. 8, pp. 8640–8655, 2021.

[25] Y. Q. Song, B. D. Obideyi, N. A. Shah, I. L. Animasaun, Y. M. Mahrous, and J. D. Chung, "Significance of haphazard motion and thermal migration of alumina and copper nanoparticles across the dynamics of water and ethylene glycol on a convectively heated surface," *Case Studies in Thermal Engineering*, vol. 26, Article ID 101050, 2021.

[26] P. Ragupathi, A. A. Hakeem, Q. M. Al-Mdallal, B. Ganga, and S. Saranya, "Non-uniform heat source/sink effects on the three-dimensional flow of Fe_3O_4/Al_2O_3 nanoparticles with different base fluids past a Riga plate," *Case Studies in Thermal Engineering*, vol. 15, Article ID 100521, 2019.

[27] B. K. Sharma, P. Sharma, N. K. Mishra, and U. Fernandez-Gamiz, "Darcy-Forchheimer hybrid nanofluid flow over the rotating Riga disk in the presence of chemical reaction: artificial neural network approach," *Alexandria Engineering Journal*, vol. 76, pp. 101–130, 2023.

[28] M. A. Z. Raja, M. Shoaib, Z. Khan et al., "Supervised neural networks learning algorithm for three-dimensional hybrid nanofluid flow with radiative heat and mass fluxes," *Ain Shams Engineering Journal*, vol. 13, no. 2, Article ID 101573, 2022.

[29] M. Shanmugapriya and P. Sangeetha, "Neural network modeling of convection heat transfer coefficient for the casson nanofluid," *TWMS Journal of Applied and Engineering Mathematics*, vol. 11, pp. 248–257, 2021.

[30] M. Elayarani, M. Shanmugapriya, and P. Senthil Kumar, "Intensification of heat and mass transfer process in MHD carreau nanofluid flow containing gyrotactic microorganisms," *Chemical Engineering and Processing: Process Intensification*, vol. 160, Article ID 108299, 2021.

[31] S. G. Krishna, M. Shanmugapriya, R. Sundareswaran, and P. S. Kumar, "MANFIS approach for predicting heat and mass transport of bio-magnetic ternary hybrid nanofluid using Cu/Al_2O_3/MWCNT nanoadditives," *Biomass Conversion and Biorefinery*, vol. 2022, pp. 1–16, 2022.

[32] S. G. Krishna, M. Shanmugapriya, A. Alsinai, and A. Alameri, "Prediction of thermal and energy transport of MHD Sutterby hybrid nanofluid flow with activation energy using Group Method of Data Handling (GMDH)," *Computational and Applied Mathematics*, vol. 41, no. 7, p. 312, 2022.

[33] M. Elayarani and M. Shanmugapriya, "Entropy minimization in non-linear radiative heat transfer of magnetized Carreau nanofluid using PSO technique," *AIP Conference Proceedings*, vol. 2516, no. 1, 2022.

[34] I. L. Animasaun, N. A. Shah, A. Wakif, B. Mahanthesh, R. Sivaraj, and O. K. Koriko, *Ratio of Momentum Diffusivity to Thermal Diffusivity, Introduction, Meta-Analysis, and Scrutinization*, Chapman and Hall/CRC, New York, NY, USA, 2022.

[35] W. Cao, A. Il, S. J. Yook, O. Va, and X. Ji, "Simulation of the dynamics of colloidal mixture of water with various

nanoparticles at different levels of partial slip: ternary-hybrid nanofluid," *International Communications in Heat and Mass Transfer*, vol. 135, Article ID 106069, 2022.

[36] A. Ishak, R. Nazar, and I. Pop, "Falkner-Skan equation for flow past a moving wedge with suction or injection," *Journal of Applied Mathematics and Computing*, vol. 25, no. 1-2, pp. 67–83, 2007.

[37] I. Ullah, I. Khan, and S. Shafie, "Heat and mass transfer in unsteady MHD slip flow of Casson fluid over a moving wedge embedded in a porous medium in the presence of chemical reaction," *Numerical Methods for Partial Differential Equations*, vol. 34, no. 5, pp. 1–25, 2018.

[38] B. L. Kuo, "Heat transfer analysis for the Falkner-Skan wedge flow by the differential transformation method," *International Journal of Heat and Mass Transfer*, vol. 48, no. 23-24, pp. 5036–5046, 2005.